The Measurement of Radar–Plasma Signatures in a Hypersonic Shock Tunnel: Simulation and Experiment

RENÉ PETERVARI
Fraunhofer Institute for High Frequency Physics and Radar Techniques (FHR), Wachtberg, Germany

STEPHAN WEIDNER
ALEXANDER NEKRIS
French-German Research Institute of Saint-Louis (ISL), Saint-Louis, France

STEFAN BRÜGGENWIRTH, Senior Member, IEEE
Fraunhofer Institute for High Frequency Physics and Radar Techniques (FHR), Wachtberg, Germany

PETER KNOTT
Fraunhofer Institute for High Frequency Physics and Radar Techniques (FHR), Wachtberg, Germany
Institute of High Frequency Technology (IHF), RWTH Aachen University, Aachen, Germany

The plasma sheath that forms around a body in hypersonic flight can change the radar signature substantially. The prediction of radar–plasma signatures, however, is complex, since it incorporates aerothermodynamics and electromagnetics and requires a number of critical assumptions on chemical and aerodynamic parameters as well as on the electromagnetic plasma model. Hence, such an approach requires thorough experimental validation to estimate and reduce its uncertainty. But radar data of hypersonic targets in free flight are extremely rare, and if existing, mostly unavailable. A different validation approach, which is common in aerothermodynamics, is to use short-time shock tunnel facilities, where for a few milliseconds, hypersonic flow conditions can be established. This article presents the adoption of this principle to the prediction of radar–plasma signatures. Under the hypersonic flow conditions inside a shock tunnel, a plasma sheath was generated above the surface of a spherical wind tunnel model and measured by an integrated experimental radar system. Afterwards, the plasma sheath and the radar signatures were simulated combining aerothermodynamic and electromagnetic solvers. Despite considerable uncertainties, good agreement between experiment and simulation was achieved.

Manuscript received 12 October 2022; revised 17 July 2023; accepted 15 August 2023. Date of publication 31 August 2023; date of current version 8 December 2023.

DOI. No. 10.1109/TAES.2023.3310497

Refereeing of this contribution was handled by M. Gashinova.

This work was supprted in part by the French and the German MoD and in part by a dedicated BAAINBw project.

Authors' addresses: René Petervari and Stefan Brüggenwirth are with the Cognitive Methods Department, Fraunhofer Institute for High Frequency Physics and Radar Techniques (FHR), 53343 Wachtberg, Germany, E-mail: (rene.petervari@fhr.fraunhofer.de; stefan.brueggenwirth@fhr.fraunhofer.de); Stephan Weidner and Alexander Nekris are with the Department for Aerodynamics, Measurements, and Simulations, French-German Research Institute of Saint-Louis (ISL), 68300 Saint-Louis, France, E-mail: (stephan.weidner@isl.eu, alexander.nekris@gmail.com); Peter Knott is with the Fraunhofer Institute for High Frequency Physics and Radar Techniques (FHR), 53343 Wachtberg, Germany, and also with the Chair of Radar Systems Engineering, Institute of High Frequency Technology (IHF), RWTH Aachen University, 52062 Aachen, Germany, E-mail: (peter.knott@fhr.fraunhofer.de). *(Corresponding author: René Petervari.)*

NOMENCLATURE

a, b, d	Distances; [m].
B	Bandwidth; [Hz].
c_0	Speed of light; [m · s^{-1}].
D	Sphere diameter; [m].
e	Electron charge; [C].
f	Radar frequency; [Hz].
f_C	(Electron) collision frequency; [Hz].
$f_{\max}$	Maximum affected frequency; [Hz].
f_P	(Electron) plasma frequency; [Hz].
f_{PRF}	Pulse repetition frequency; [Hz].
f_S	Sampling frequency; [GS · s^{-1}].
f_0	Lower band limit frequency; [Hz].
g, l	Indices; [-].
h	Specific enthalpy; [MJ · kg^{-1}].
H	Altitude; [km].
$H(r)$	Range transfer function; [-].
i	Species $\in$ {N_2, O_2, N, O, NO, NO^+, e^-}.
k_B	Boltzmann's constant; [kg · m^2 · s^{-2}K^{-1}].
m_e	Electron mass; [kg].
M	Reaction partner $\in$ {N_2, O_2, N, O, NO, NO^+}.
Ma	Mach number; [-].
n	Refractive index; [-].
$n(i)$	Number density of species i; [m^{-3}].
p	Pitot pressure; [Pa].
ϵ_0	Electric field constant; [As/V/m].
r	Range; [m].
R, R_N	Radius, nose radius; [m].
RCS	Radar cross section; [m^2].
$s^2(r)$	Radar range profile; [m^2 · m^{-1}].
$S^2(f)$	RCS spectrum; [m^2].
t	Time; [s].
T_e	Electron temperature; [K].
T_s	Total/stagnation temperature; [K].
T_t	Translational, static temperature; [K].
T_v	Vibrational, static temperature; [K].
U	Velocity; [m · s^{-1}].
$\bar{v}_e$	Average electron velocity; [m · s^{-1}].
x, y, z	Spatial coordinates; [m].

Δt_{start}	Time required for establishment of stationary flow conditions; [s].
ϵ_r	Relative permittivity; [-].
$\mathcal{F}$	Fourier transform operator; [-].
λ	Wavelength; [m].
η	Visualization adjustment factor; [-].
ρ	Density; [g · m^{-3}].
$\sigma^{mat}_{sim/meas/ref}$	RCS error estimate; [m^2].
Σ	Visualization of plasma caused RCS change; [-].

I. INTRODUCTION

Due to the emergence of new hypersonic threats [1] and the growing proliferation of ballistic missiles [2], there is an increasing need for respective countermeasures. Because of their long ranges and all-weather-capabilities, radar systems are a vital component for the detection, tracking and identification of hypersonic threats as well as the guidance of countermeasures. Any uncertainty about the reflection properties of hypersonic targets can have severe consequences, and thus, must be avoided.

A central feature of hypersonic flight (Mach number $Ma > 5$) is the presence of a plasma sheath around high-speed bodies at sufficiently high Mach numbers, flow temperatures, and densities. Plasma is formed by ionizing chemical reactions of the air molecules in high-temperature regions along the body surface. These high-temperature regions are caused by the strong compression across the shock wave (shock-wave heating) and viscous dissipation in the boundary layer, both typical for the hypersonic flight domain [3, pp. 13–31 and 460]. Plasma is not electromagnetically neutral and shows the behavior of a lossy, dielectric, dispersive medium [4, p.136]. As such, it influences the deflection and absorption of incoming electromagnetic waves, like microwaves used in radar systems.

Until today, some efforts have been made to identify the impact of a plasma sheath on microwave propagation. Besides radar signatures of hypersonic targets, also the study of the radio communication blackout during the atmospheric reentry is an important application area. Three main approaches have been established to solve the electromagnetic interaction with a known plasma sheath. First, considering the plasma sheath as layered medium with constant plasma values in each layer [5], [6], [7], [8], second, applying ray tracers [9], and third, solving the electromagnetic wave propagation in plasma with rigorous numerical approaches like finite-difference time-domain (FDTD) solvers [10], [11], [12], [13]. These solutions, however, are not exact and use some approximations like a rectangular grid in usual FDTD schemes or require further assumptions like the absence of a magnetic field to simplify the considerations.

Furthermore, each of the aforementioned techniques requires information about the shape of the plasma and the distribution of the plasma parameters, which are derived from aerothermodynamics either by numerical simulations or proper assumptions. Hence, they rely on accurate predictions of relevant plasma parameters like electron density and particle densities of molecular and atomic species. These result from temperature-sensible chemical reaction rates and the respective collisional cross sections in high-temperature air, which are still to some degree uncertain [14], [15] and have been an active field of research until today [16]. Given these uncertainties, experimental reference data are necessary to provide reliable predictions.

Other than for central aerodynamic parameters like temperature or pressure, there are no standard techniques to measure these microscopic quantities directly and relevant experimental data for validation are thus rare. It relies mainly on a few reentry flight experiments from the late 60 s and early 70 s with a 9° half-angle sphere cone [17]. A good reference for the validation of electron densities is the RAM C-II flight experiment [18], [19], which was originally designed to study the radio communication black out during the atmospheric reentry. The radar cross section was studied in a later flight experiment during the Trailblazer campaign with a ground based radar [20]. The complexity of such experiments is high—not only in preparation but also in flight. Multiple effects like turbulence, ablation, or body motion happen at the same time and under changing atmospheric conditions thus rendering it difficult to separate them in the data to get further insights. The conditions are not fully controllable and cannot be repeated easily. The same applies to another common source of reference data: the observation of targets of opportunity like reentering meteorites or space debris [21], [22], where even the presence cannot be guaranteed.

To study the hypersonic regime, ground-based test facilities like shock tunnels have been established [23]. Although, hypersonic flow conditions are achieved only for short times, experiments can be repeated more often, and model orientation as well as flow conditions can be set more freely and repeatable. Hypersonic wind tunnels also have some drawbacks since they introduce freestream disturbances, and hence, flow conditions can show some fluctuations [3, p. 330] as well as freezing of the vibrational energy modes within the nozzle [3, p. 667]. By simulating the flow generation process and measuring reference values during each test, these newly introduced uncertainties can, however, be reduced. Although, it is not possible to exactly reproduce the conditions in hypersonic flight in a shock tunnel, all important physical effects for the scope of this study (surface heating, plasma formation, and interaction with radar waves) can be reproduced. Hence, radar measurements of bodies with plasma sheaths in hypersonic wind tunnel flows could provide the missing reference data that is required to validate the aforementioned simulation of radar–plasma signatures. A first study employing microwave radiation for electron density measurements in a hypersonic shock tunnel is documented in [24].

Although radar has a long-standing tradition in the observation of high-temperature plasmas, especially for nuclear fusion [25], it is no standard technique in hypersonic wind tunnels. To the authors' best knowledge, [26] is the only other reference in open literature that provides experimental radar data of a hypersonic plasma sheath acquired

in a ground-based test facility. Due to the lack of calibrated radar cross section (RCS) data, a quantitative validation of radar simulation software was not possible, based on the published data. Data for validation would require the following:

1) A clear definition of test conditions (freestream quantities, geometries etc.);
2) A simple geometry to facilitate the modeling and to reduce the complexity in electrodynamic and aerodynamic simulations;
3) Quantitative, calibrated RCS measurements;
4) A set of varying conditions with relevant RCS changes.

Addressing the aforementioned points, a shock tunnel experiment was designed and proven feasible by numerical analysis [27]. Following the same numerical approach, a combination of computational fluid dynamics (CFD) and electromagnetic simulations (FDTD) was established with the aim of high-confidence predictions of radar–plasma interaction. This article gives a detailed description of the conducted shock tunnel experiments and compares the measured radar–plasma signatures with the respective numerical predictions based on the approach described in [27].

II. THEORY

A. Aerodynamic Plasma Generation

Aerodynamic plasma formation during the atmospheric reentry is caused by chemical reactions in high-temperature air. These high-temperature regions originate from flow compression due to the present shocks and viscous dissipation in the flow along high-speed bodies where strong velocity gradients occur and kinetic energy is dissipated into heat. Following [3, p. 590], at temperatures below 9000 K, the most important reactions are

$$\mathrm{N_2 + M \leftrightarrow 2N + M} \tag{1}$$
$$\mathrm{O_2 + M \leftrightarrow 2O + M} \tag{2}$$
$$\mathrm{NO + M \leftrightarrow N + O + M} \tag{3}$$
$$\mathrm{NO + O \leftrightarrow O_2 + N} \tag{4}$$
$$\mathrm{N_2 + O \leftrightarrow NO + N} \tag{5}$$
$$\mathrm{N_2 + O_2 \leftrightarrow 2NO} \tag{6}$$
$$\mathrm{N + O \leftrightarrow NO^+ + e^-} \tag{7}$$

where M can be any of the molecules present in the flow. In total, seven species are involved: N_2, O_2, N, O, NO, NO^+, and e^-. Simulations have shown that in the considered range of experimental conditions, temperatures will not exceed 9000 K. The last reaction (7) is responsible for plasma formation in this temperature range [28].

B. Electromagnetic Plasma Model

In this article, the simplified plasma dispersion model, is applied, which was derived in the feasibility study [27]. It is an implementation of the Drude model and incorporates a seven-species thermochemical model ($i \in \{\mathrm{N_2}, \mathrm{O_2}, \mathrm{N}, \mathrm{O}, \mathrm{NO}, \mathrm{NO^+}, \mathrm{e^-}\}$) to calculate the central parameters for the permittivity of the relevant electron plasma

$$\epsilon_r = 1 - \frac{f_P^2}{f^2\left(1 - j\frac{f_C}{2\pi f}\right)} \tag{8}$$

which are the (electron) plasma frequency

$$f_P = \frac{1}{2\pi}\sqrt{\frac{n(e^-)e^2}{\epsilon_0 m_e}} \tag{9}$$

and the (electron) collision frequency

$$f_C = \sum_{i=1}^{7} n(i)\bar{v}_e \pi \bar{\Omega}_{ei}^{(1,1)} \tag{10}$$

with

$$\bar{v}_e = \sqrt{\frac{8k_B T_e}{\pi m_e}} \tag{11}$$

$$\pi \bar{\Omega}_{ei}^{(1,1)} = e^D T_t^{A(\ln T_t)^2 + B\ln T_t + C} \tag{12}$$

where (11) represents the average thermal velocity of the electrons and (12) the respective collision integral with Gupta's correlations for electron reactions (index e) with particle species (index i) in high-temperature air [14]. The remaining variables denote the frequency f of the considered electromagnetic wave, the translational component of the temperature T_t, the electron charge e, electron number density $n(e^-)$, the electric field constant ϵ_0, the electron mass m_e, Boltzmann's constant k_B, and the electron temperature T_e. The variables A, B, C, and D are tabulated values from [14]. Here, the following simplifications were made:

1) The electron temperature is low enough to treat the aerodynamic plasma as a cold plasma ($T_e < 10\,000$ K);
2) The motion of the ions is by several magnitudes smaller than that of the electron plasma and is omitted;
3) The vibrational component of the temperature is neglected and all translational temperatures of each species are in local equilibrium yielding a single ambient temperature T;
4) The Earth's magnetic field is negligible and the plasma is, hence, nonmagnetic and isotropic;
5) The ambient density is too low to affect the microwave propagation significantly and the ambient permittivity is omitted and set to 1.

The feasibility study [27] showed that these assumptions are reasonable for the aimed experimental conditions at 40-km altitude and a velocity of 4 km $\cdot$ s^{-1}.

Analyzing the plasma dispersion relation yields some important insights to the reflection properties of plasma, and hence, the experimental setup. If the collision frequency f_C is negligible, the dispersion relation simplifies to

$$\epsilon_r = 1 - \frac{f_P^2}{f^2}. \tag{13}$$

And further, if the local electron density $n(e^-)$ is high enough that the plasma frequency f_P exceeds the frequency f of an impinging electromagnetic wave, ϵ_r becomes negative. Since these waves are not generated within the plasma but must always penetrate some kind of interface, continuity necessitates the presence of a surface where $\epsilon_r = 0$. A refractive index $n = \sqrt{\epsilon_r}$, governing the wave propagation inside media, means that no wave can propagate beyond an $\epsilon_r = 0$ isosurface. This requires total reflection, a behavior similar to a metallic surface. Hence, if density and temperature are low, so are the local number densities $n(i)$ and collisional cross sections $\bar{\Omega}_{ei}^{(1,1)}$, and thus, also the collision frequency f_C. Straightforward calculations show that even moderate collision frequencies do not change this behavior until f_C exceeds the radar's frequency f. With the aimed conditions resembling an altitude of 40 km, density and temperature are adjusted to achieve high reflection. For the experiment, this has some advantages since monostatic radar measurements, as applied here, rely on reflections. By reducing the reflection of the background structure, here the model, the signal-to-noise ratio coming from the plasma can be increased.

In general, however, plasma will not always maximize the reflection. Depending on the relation between plasma frequency and collision frequency, plasma can also be highly absorptive or simply transparent [29].

III. EXPERIMENT

For the purpose of providing experimental reference data for validating simulation software for radar–plasma signatures, hypersonic shock tunnel experiments were conducted. Following the design in [27], a spherical wind tunnel model was placed in the Mach 8 hypersonic flow of the Shock Tunnel B (STB) at French-German Research Institute of Saint-Louis (ISL). Plasma was generated in the high-temperature region around the stagnation point of the sphere and the change of microwave reflectivity was observed with a radar system. Simultaneously, the emission of light coming from the high-temperature regions was observed with a synchronized high-speed camera system as reference. Each of the different experimental aspects is covered in detail as follows.

A. Model

The choice of the model geometry, material, and manufacturing process was lead by the conditions inside the wind tunnel and the knowledge about the interaction of radar waves with the model and the plasma sheath.

Besides its simple definition and the absence of an angle-of-attack in the flow, a spherical geometry has the advantage of the available analytical electromagnetic solutions for easier calibration. The feasibility study [27] showed that for a 15-cm sphere under the aimed conditions (40-km altitude and a velocity of 4 km $\cdot$ s^{-1}), plasma can increase the reflectivity to total reflection in the used frequency band (3 to 15 GHz) in the high-temperature regions around the stagnation point. The size of the model and its geometry is thus sufficient for relevant plasma production.

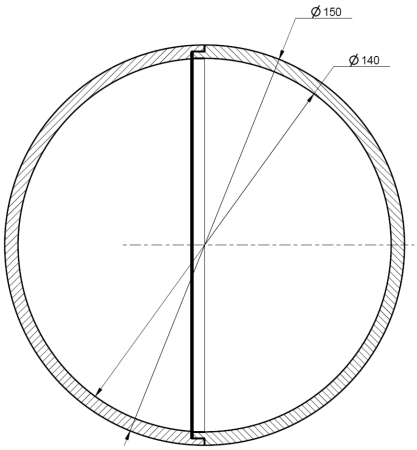

Fig. 1. Cross section of the spherical shell model manufactured by two hemispherical shells with tight fit. Units in millimeter.

Hence, under the conditions inside the wind tunnel, in front of the model, a reflective layer will emerge, whose surface will be shaped similar to the sphere underneath. If the model was made of metal, the emergence of plasma would barely have altered the total reflectivity, because the surface of total reflection would only be displaced from the sphere's metallic surface to the edge of the thin plasma layer on top. The change in geometry would be marginal, and thus, the measurable effect. To increase the signal-to-noise ratio measured by the radar system, two low reflective materials were used instead: Teflon (PTFE, $\epsilon_r = 2.1$) and Polyamide (PA, $\epsilon_r = 2.33$). Due to the vacuum conditions before each test and the related danger of inflation, closed cell material with even less permittivity like styrofoam could not be used. Furthermore, the structure needed to withstand the high acceleration caused by the incoming 4 km $\cdot$ s^{-1} flow at least during the test time. PTFE and PA both meet these requirements. However, by using a material, which is low-reflective, and thus, semitransparent for microwave radiation, the radar waves can penetrate the model and can be reflected also inside the sphere. But, given high enough resolution, the reflection in the front influenced by plasma can be separated from the trailing edge reflection.

The spherical test body was suspended by thin PA threads (nylon) attached to the model, since any mounting structure in the radar beam would not only disturb the flow but also the radar measurements. To reduce the weight and make the suspension with nylon threads feasible, a hollow sphere design with 5-mm thick walls was chosen. The technical drawing of the two assembled hemispherical shells is shown in Fig. 1.

The 150-mm diameter also suits the resolution capabilities of the radar system. At the best range resolution of 1.25 cm using the full 12-GHz bandwidth, the sphere can be easily resolved in more than ten resolution cells; sufficient for separating the different scattering contributions of a semitransparent spherical shell.

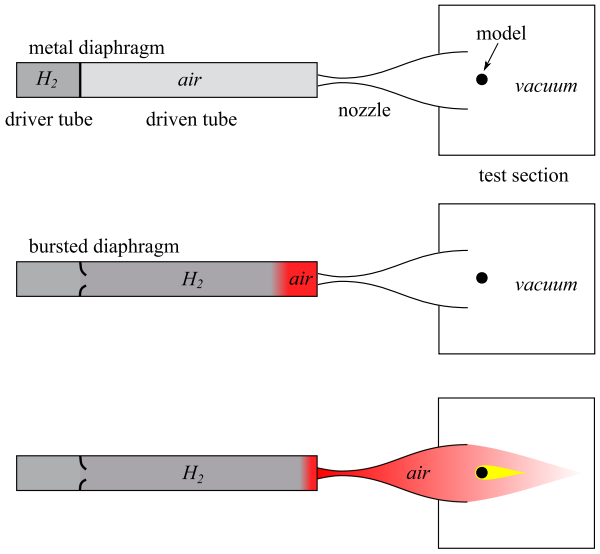

Fig. 2. Principle of operation of ISL's STB.

B. Shock Tunnel

This article considers experiments conducted at ISL's shock tube laboratory. The shock tunnel B (STB) is capable of providing up to 8 MJ · kg^{-1} to conduct high enthalpy flow experiments [30]. The facility is composed of a shock tube with a Laval nozzle connected to the end of the driven tube, followed by a measurement chamber and a dump tank. The inner diameter of STB's shock tube amounts to 100 mm. Its driver tube is 4.0-m long and the driven tube measures 18.4 m.

The operation principle is shown schematically in Fig. 2. Before each test, high pressure hydrogen is filled into the driver tube. It is separated from the driven tube by a metal diaphragm. Dry air (21mol% O_2, 79mol% N_2) is used as test gas. A second diaphragm made of polymer prevents the test gas from flowing through the nozzle into the evacuated test section before the start of the shock tunnel experiment. When the metal diaphragm bursts, a strong shock wave runs through the shock tube compressing, and thus, heating the test gas. When the shock arrives at the end of the tube, the shock gets reflected—further heating and compressing the test gas—and the polymer diaphragm ruptures. The compressed and heated test gas is afterwards expanded through the nozzle. Due to its characteristic shape as well as the large pressure difference between the high-temperature air upstream of the nozzle and the vacuum in the test section, the nozzle transforms the high enthalpy at the end of the tube into kinetic energy. Thereby, it creates short-time, quasi-steady-state hypersonic flow conditions in the test section of the wind tunnel.

C. Radar System

To observe the plasma formation, FHR's Multi Application Software Defined Radar (MASoDeRa) system was used. It consists of an arbitrary waveform generator (AWG, Tektronix AWG70001A) for signal generation, an high performance oscilloscope (OSC, Tektronix DPO77002SX)

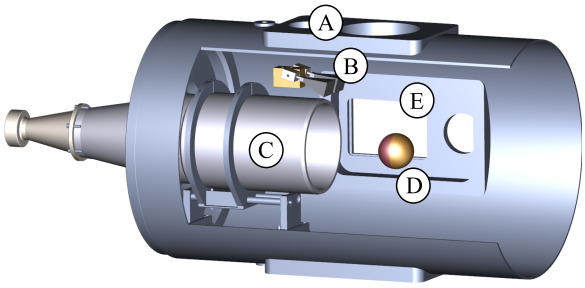

Fig. 3. Experimental setup inside the test section: vacuum feeds (A), antennas (B), hypersonic nozzle (C), wind tunnel model (D), and test section window (E).

and (in this configuration) two standard gain horn antennas for operation in the 2–18 GHz band, one for transmit and one for receive. Considering the operation inside a shock tunnel, a variety of difficulties arise from the small space, the metallic surfaces, the vacuum before the test, the short test time, and the harsh conditions, which include the following:

1) Antennas must be placed outside the flow to avoid damage;
2) Vacuum feeds for the antenna cables are required to maintain electromagnetic transmission and a stable vacuum condition in the test section at the same time;
3) Metallic walls and structures contribute to a complex background, which must be corrected for and removed or covered if possible;
4) The small space inside the test section demands the proximity of the model to the antennas, far-field assumptions may be stretched;
5) Due to the short test durations high pulse repetition rates (PRF) and accurate triggering with low latency are required.

Addressing these circumstances, the antennas were placed in a quasi-monostatic configuration just above the nozzle, illuminating the sphere and its wake with an approximate width of the main beam between ±10° and ±20° depending on the frequency. The incidence of the wave fronts on the stagnation point on the sphere was approximately 45° with respect to the wind tunnel axis (see Fig. 3). To maintain a stable vacuum before each test run, vacuum feeds for the antenna cables were designed. Furthermore, metallic structure was covered as far as possible by broad band absorbers to reduce the background. Using the full bandwidth of the antennas, the system operated a linear-frequency-modulated chirp waveform from 3 to 15 GHz providing a range resolution of 1.25 cm. The waveforms were sampled directly without downconversion. The short test times were addressed by a high PRF of $f_{\mathrm{PRF}} = 250\mathrm{kHz}$, i.e., 250 pulses per millisecond. The memory limited the maximum acquisition time to 20 ms. An overview of the set of system parameters is given in Table I. Each waveform was transformed into a range profile using inverse filtering. Fig. 5 shows a typical set of radar range profiles before the flow arrival and during the test time. The microwaves are first reflected at the front at 35 cm. Since PTFE and PA

TABLE I
System Parameters

Parameter	Value
Sampling frequency f_S (Tx and Rx)	50 GS s^{-1}
AWG min. waveform size	4800 S
Pulse repetition frequency f_{PRF}	250 kHz
Frequency band $[f_0, f_0 + B]$	3 to 15 GHz
OSC memory	50 MS
OSC acquisition time (at $f_{PRF} = 250$ kHz)	20 ms

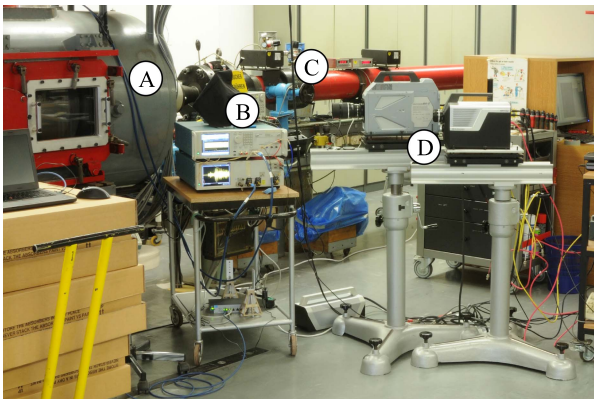

Fig. 4. Setup view from outside the test section: the test section (A), the MASoDeRa system (B), the shock tube (C), and the high-speed cameras (D).

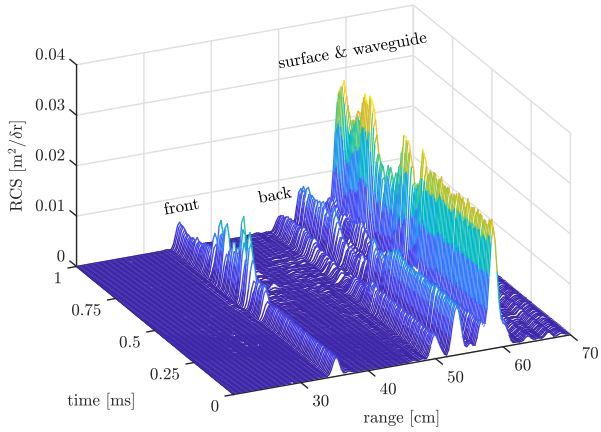

Fig. 5. Typical temporal evolution of radar range profiles showing every second profile. Test time is between 0.6 and 0.7 ms.

are semitransparent for microwaves, the wave penetrates the surface of the sphere and is reflected at the back, one diameter behind, at 50 cm. The subsequent reflections result from waveguide effects in the 5-mm wall of the sphere and surface waves. For the peaks behind the front reflection peak, the incoming radiation is already disturbed and can cause further deviations. For the purpose of a validation experiment, the front reflection peak appears thus most suitable and is extracted for all subsequent analyses. It can already be observed that the plasma shows the desired behavior increasing the front reflection. At the same time, this increased reflection leads to a suppression of all subsequent scatterers.

D. Camera System

Due to the strong heating in the stagnation point, the flow will emit light, which can be observed by high-speed cameras. For the present experiments, timing was critical. Hence, a high-speed camera system (Shimadzu HPV-X2, Fig. 4) was used as reference to observe the establishment of the flow and the simultaneous generation of plasma independently from the radar system. For this purpose, the camera was synchronized with the radar's PRF of 250 kHz.

While the emitted light is useful for determining the flow state on the object, it also raises the question of its origin. Recent spectrometer measurements in a free-piston shock tunnel [31]—the JAXA HIEST—showed a heat flux bias of more than 10% due to radiative heating by heavy metal atomic impurities, primarily iron, in the free stream flow for specific enthalpies larger than 10 MJ $\cdot$ kg^{-1}. Although the operating principle is slightly different for the reflected shock tunnel used in this study and the heat flux bias has been shown to be negligible at 8 MJ $\cdot$ kg^{-1} [31], it is known that the shock tunnel used in this study also has metal impurities in its free stream flow. Whether these impurities affect the plasma generating chemical reactions, and hence, the radar measurements, would require additional spectrometer measurements and respective simulations. This, however, is beyond the scope of this study and should be addressed in a separate investigation.

E. Test Conditions

For this article, shock tunnel runs with specific enthalpies between 4 and 8 MJ $\cdot$ kg^{-1} in the nozzle supply chamber were conducted. The highest condition was also considered in the feasibility study [27] resulting in a freestream flow velocity of $U = 4$ km $\cdot$ s^{-1} with the pressure, temperature, and density approximating the U.S. Standard Atmosphere [32] conditions at 40-km altitude. For the highest specific enthalpies investigated in this article, the freestream temperature T exceeds the typical ambient temperature at this altitude by up to 430 K, but compared to the stagnation temperature T_s in the order of a few thousand K (see Table II), this deviation is negligible. Hence, the results are still relevant for this altitude and geometry. The given values in Table II result from calculations with the equilibrium shock tube code (ESTC) [33] based on the initial shock tube fill conditions as well as the shock speed and the nozzle-supply pressure, measured before and during the tunnel run.

F. Test Time Determination

Due to the short test times, timing is critical for these experiments. During each test run, the flow along the sphere passes through three stages: the nozzle starting process, the test time, when the nozzle is in relatively stable operation, and the unstable after flow. Three independent sensor types have been used to determine the current flow condition: pressure sensors in the nozzle supply chamber and at the nozzle end, the radar system, and the camera system. To determine the test time interval, Fig. 6 shows the normalized

TABLE II
Estimation of the Test Conditions With ESTC [33] Based on Measured Shock Tube Fill Conditions, Shock Speed, and the Nozzle Supply Pressure After the Shock Reflection for the Individual Tunnel Runs

Cond.	h [MJ kg^{-1}]	T_s [K]
4	8.00	4912
5	8.14	4973
6	4.35	3327
7	4.49	3446
8	5.08	3727
9	5.73	3995
10	5.86	4044
11	6.07	4114
12	6.73	4376
13	7.01	4490
14	7.18	4574

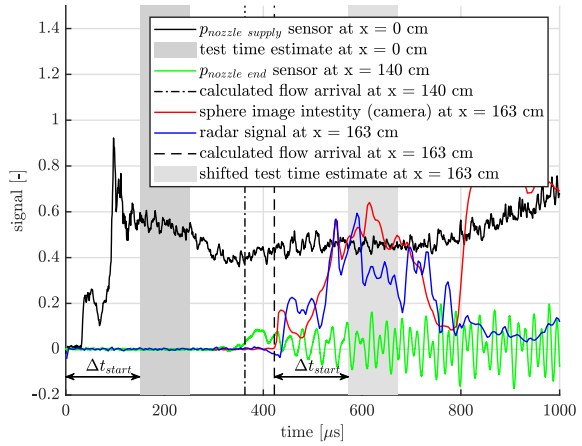

Fig. 6. Combination of the normalized time signals at their respective distance x from the nozzle throat at the example of run five to determine the test time window.

signals coming from these sensors exemplarily for run 5. The pressure signal was used directly, whereas from the radar signal only the sphere's front reflection was extracted (compare Fig. 5) and from the camera the gray-scale value integrated across each frame was used. At first, the flow arrives at the pressure sensor at the nozzle inlet $p_{\text{nozzle supply}}$ at $x = 0$ cm and all systems are triggered ($t = 0$ μs). After the nozzle starting phase ($\Delta t_{\text{start}} \approx 150$ μs), the conditions enter the stable test phase $t = [150\ \mu\text{s}; 250\ \mu\text{s}]$, which will be used as test conditions when they arrive at the model 163-cm downstream of the nozzle throat. Before, the flow arrives at the pressure sensor at the nozzle end $p_{\text{nozzle end}}$ at $x = 140$ cm, here at $t = 377$ μs. As shown in Fig. 6, due to strong oscillations, the $p_{\text{nozzle end}}$ sensor does not provide meaningful pressure data. However, the start of the oscillation agrees well with the arrival of the initial shock wave at the sensor and it is likely to be caused by it. It appears, hence, reasonable to use the onset of the vibrations to support the estimation of the radar test time on the model. After the time delay of approximately 50 μs caused by the 23-cm distance between the nozzle end and the front of the sphere, a simultaneous response in the

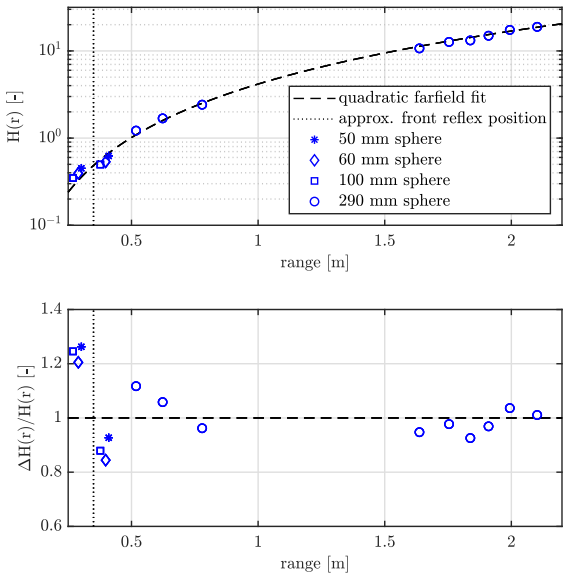

Fig. 7. Range transfer function $H(r)$ and the relative deviation from the r^{-2}-law.

camera and radar signal is observed. The stable test phase time window relevant for the radar and the camera thus shifts to $t = [570\ \mu\text{s}; 670\ \mu\text{s}]$ after trigger. The agreement of the three different sensor types supports the choice of the correct test time window.

G. Near-Field Measurements

Measuring the RCS of a target in close proximity to the antennas comes with some difficulties. However, due to the limited size of the test section, there is no space for larger distances and far-field conditions may be stretched. To investigate the impact, the range dependence of the amplitude has been measured inside an anechoic chamber. Four metallic spheres with different diameters (50 mm, 60 mm, 100 mm, and 290 mm) were measured at different distances r from the antennas. Using the theory of linear time-invariant systems, the properties of the radar are absorbed into a transfer function $H(r)$ relating the measured signal $Y(r)$ with the ideal response $S(r)$ in 1-m distance. In the far-field the amplitude must decay as r^{-2}. In Fig. 7, the measurements of the range transfer function $H(r)$ are given together with its deviation $\Delta H(r)$ from the r^{-2} law. Apparently, the r^{-2} free-space loss correction is a good approximation, also in the close region, where the sphere will be placed. However, the higher scatter relative to the absolute value of $\Delta H(r)/H(r)$ in the close region also results in a higher uncertainty up to $\pm 30\%$ of the finally measured absolute RCS values of the sphere's front reflection. Angle inaccuracies during the calibration measurements are likely to have caused this problem.

H. Unit Considerations

Since the data shall be used as reference, units must be defined unambiguously. The natural unit of the squared spectrum $S^2(f)$ is the RCS in m^2 for a given frequency f.

The unit of the profile follows from the Fourier transform, implemented as `fft`:

$$\left[\mathcal{F}^{-1}(S(f))\right] = \left[\int_{-\infty}^{\infty} S(f)\exp(j2\pi ft)\mathrm{d}f\right] = \mathrm{ms}^{-1} \quad (14)$$

$$\approx \left[\sum_{l}^{L} S(f_l)\exp(j2\pi \tfrac{l}{L}g)\tfrac{1}{L\Delta t}\right] \quad (15)$$

$$= \left[s(t_g = g\Delta t)\right]. \quad (16)$$

Rescaling the axis with $\Delta t = 2\Delta r/c_0$ yields the natural unit of the squared range profile

$$\left[s^2(r_g = \tfrac{t_g c_0}{2})\right] = \mathrm{m}^2/\Delta r \quad (17)$$

where the ordinate integration measure unit Δr remains unaffected. When the `fft` is fully occupied across the bandwidth B the returned range resolution

$$\Delta r = \frac{c_0}{2}\Delta t = \frac{c_0}{2}\frac{1}{B} = \delta r \quad (18)$$

coincides with the physical resolution δr. To smoothen the profiles coming from the `fft` and to get an impression of the point spread function, the spectra were zero padded such that the new resolution $\Delta r'$ and δr do not coincide anymore. The padding ratio η changes the ratio into

$$\Delta r' = \frac{c_0}{2}\Delta t = \frac{c_0}{2}\frac{1}{\eta B} = \frac{\delta r}{\eta}. \quad (19)$$

To identify the peak value in the range profile with the mean value of the spectrum, the unit of the range profile was changed accordingly to

$$\left[\eta s^2(r_g)\right] = \eta\mathrm{m}^2/\Delta r = \mathrm{m}^2/\delta r. \quad (20)$$

IV. AERODYNAMIC SIMULATION

To verify the combined aerodynamic-electromagnetic simulation approach described in [27], the experimental flow conditions and the respective radar response were simulated for each test case. Besides a precise understanding of the behavior of the flow helping to interpret the experiments, the aerodynamic simulations provide detailed distributions of thermodynamic and plasma parameters, which are inevitable for the following simulation of the radar–plasma interaction.

A. Model and Solver

The fluid flow is simulated by numerically solving the mass, momentum and energy conservation equations using a finite-volume method approach. The turbulence is modeled by means of two further conservation equations for the turbulent kinetic energy k and the specific dissipation rate ω based on the k–ω shear-stress transport (SST) model [34]. Additionally, to account for the chemical reactions, species conservation equations for each of the seven species [15] considered in this study are solved. An implicit, first-order accurate Euler method was used for the time discretization, whereas the spatial discretization was second-order accurate. For this article, the open-source *hy2Foam* solver [35] was chosen, supporting chemical nonequilibrium occurring during atmospheric reentry. Compared to the high flow velocity, reaction rates can be too slow to reach a local chemical equilibrium. A detailed description of chemical nonequilibrium in hypersonic flows may be found in [3, p.575]. To respect the complexity of hypersonic flows, Park's two-temperature model with a single vibrational energy pool [15] is used together with the transport model of Blottner and Eucken [36], [37], Fick's diffusion law, the mixing rules of Armaly and Sutton [38], and corresponding collision data from [39].

B. Mesh and Boundary Conditions

The aim of the aerodynamic simulation is to provide best possible predictions for the flow conditions encountered during the wind tunnel runs. For this purpose, besides the setup in the test section, the process of hypersonic flow generation across the nozzle is included in the simulation. The computational grid used is shown in Fig. 8. For the reduction of complexity, axisymmetric flow is assumed and the calculations are carried out on a quasi-2-D wedge slice of the volume. The mesh is a structured grid, which consists of 5.8×10^4 control volumes. The meshed geometry consists of the nozzle supply chamber of the shock tunnel, the Mach 10 convergent-divergent nozzle and the test section with the sphere in it. A fixed velocity, pressure, temperature, turbulent properties, and species concentration inlet boundary condition is defined upstream of the nozzle supply chamber according to ESTC [33] calculations based on the measured experimental conditions. At the downstream end of the test section, behind the spherical body, a zero-gradient outlet boundary condition is applied. The remaining domain boundaries are consistently set to isothermal, noncatalytic walls in translational, and vibro-electronical thermal equilibrium. The flow field was initialized with the experimentally determined nozzle supply conditions upstream of the nozzle throat and a near vacuum condition downstream of the throat. To verify the resolution of the computational grid used, a grid refinement study was conducted. A refined CFD grid was created by subdividing each individual computational cell into four cells. The region close to the shock wave was found to be most sensitive to changes in grid resolution. In absolute values, however, the deviations are below the detection threshold of the radar system. Therefore, these deviations do not affect the radar simulation and the flow is sufficiently well resolved by the grid used.

C. Validation

1) *Pitot Study:* For validation, prior to the radar measurements, several test runs with ten Pitot pressure probes positioned 50-mm downstream of the nozzle, at different radial positions with respect to the wind tunnel axis, were conducted at specific enthalpies h of 6 $MJ \cdot kg^{-1}$ and $7MJ \cdot kg^{-1}$, respectively. Two of these test runs were then calculated exemplarily, using the same numerical setup as described in Sections IV-A and IV-B. Usually, it is not necessary to include the Pitot pressure tubes into the

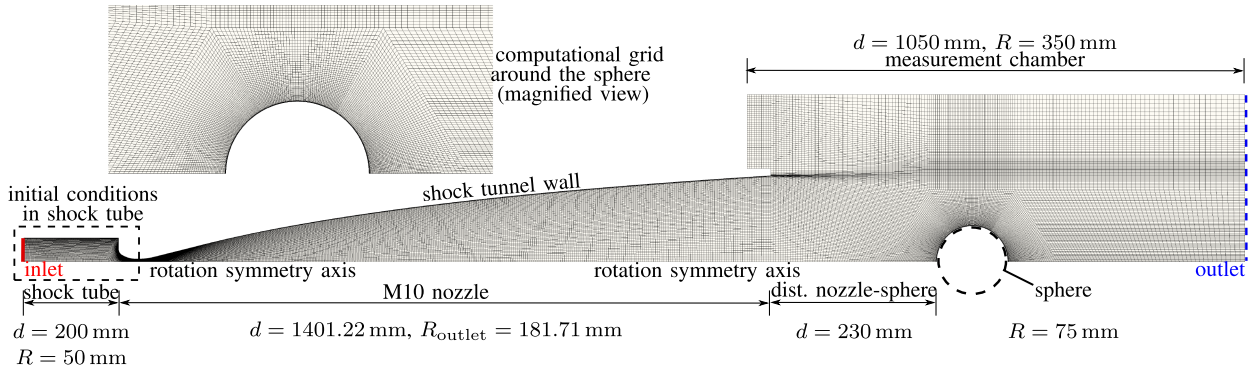

Fig. 8. Computational grid.

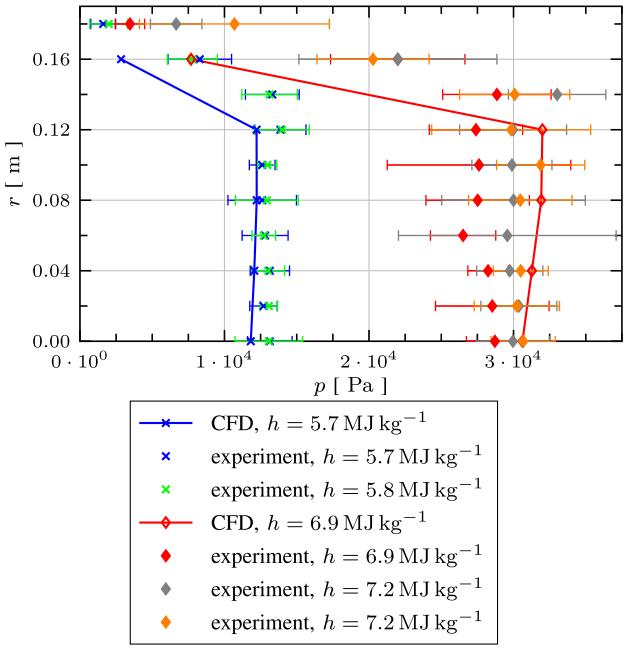

Fig. 9. Radial Pitot pressure profiles 50-mm downstream of the nozzle end for two wind-tunnel runs at approximately $6MJ \cdot kg^{-1}$ and three tunnel runs at approximately $7MJ \cdot kg^{-1}$ compared with two numerical simulations of the nozzle flow, one for each specific enthalpy regime.

numerical simulation domain, since the Rayleigh Pitot tube formula can be used to calculate the Pitot pressure from the freestream static pressure and the freestream Mach number [40]. In the present case, this is not possible, since the Rayleigh Pitot tube formula is only valid for an ideal gas and cannot account for the real gas effects, i.e., changing heat capacity ratios, occurring behind the shocks caused by the Pitot probes. Therefore, an additional axisymmetric computational mesh was generated comprising the geometry of the Pitot probes used in the experiments. In contrast to the experiments, only every second Pitot probe was modeled in the mesh.

Fig. 9 compares the measured and the simulated Pitot pressures, showing acceptable agreement when considering the high measurement uncertainties caused by the fluctuating flow conditions. The experimental results show a decrease of the Pitot pressure for radii larger than 0.14 m, corresponding to the momentum thickness of the nozzle boundary layer.

2) *RAM C-II:* Moreover, the prediction capabilities of the numerical simulations for microscopic plasma parameters were assessed. Therefore, the RAM C-II flight vehicle having a nose radius R_N of 0.1512 m, a cone half-angle of 9° and a total length of 1.2954 m [17] was simulated using the same setup as described in Section IV-A, however, assuming a laminar flow. A structured quasi-axisymmetric wedge-grid comprising 75.5×10^3 cells was used. The inlet boundary conditions were set to a freestream velocity of 7636.4 $\mathrm{m \cdot s^{-1}}$, a thermal-equilibrium freestream temperature of 254 K and a freestream static pressure of 19.85 Pa according to the freestream conditions given by Tchuen and Zeitoun [41] for an altitude of 61 km, which, however, slightly differ from the 7651 $\mathrm{m \cdot s^{-1}}$ reported by Jones and Cross [17] and the 243 K and 17.66 Pa of the standard atmosphere conditions [32]. The molar fractions at the inlet were set to 79 mol% N_2 and 21 mol% O_2. A zero gradient outlet boundary condition was used since the outlet was located sufficiently downstream of the vehicle and the flow left the computational domain at supersonic speed. Since no temperature data were acquired during the free-flight campaign, respective estimations are necessary. Hence, the surface of the vehicle is considered a no-slip, no-temperature jump, chemically noncatalytic wall at a temperature of 1500 K [41], which corresponds to the upper limit of the typically assumed wall temperatures for the RAM C-II vehicle [16]. Directly at the wall, the flow is considered in thermal equilibrium. Fig. 10 compares the simulated electron density at 61-km altitude, i.e., the maximum perpendicular to the vehicle surface, with experimental data [17], [18] and numerical simulation results from the literature [16], [42]. The reflectometer measurements give the altitudes at which the reflected signals of the individual radar frequencies (S, X, and Ka band) were exceeding or falling below a threshold, which could then be linked to a governing plasma frequency and hence the electron density [18]. Fig. 10, therefore, gives both, the discrete values closest to 61-km altitude and the range of possible interpolations between these data points. For $x/R_N = 0.30$, the reflected Ka band signal exceeded the

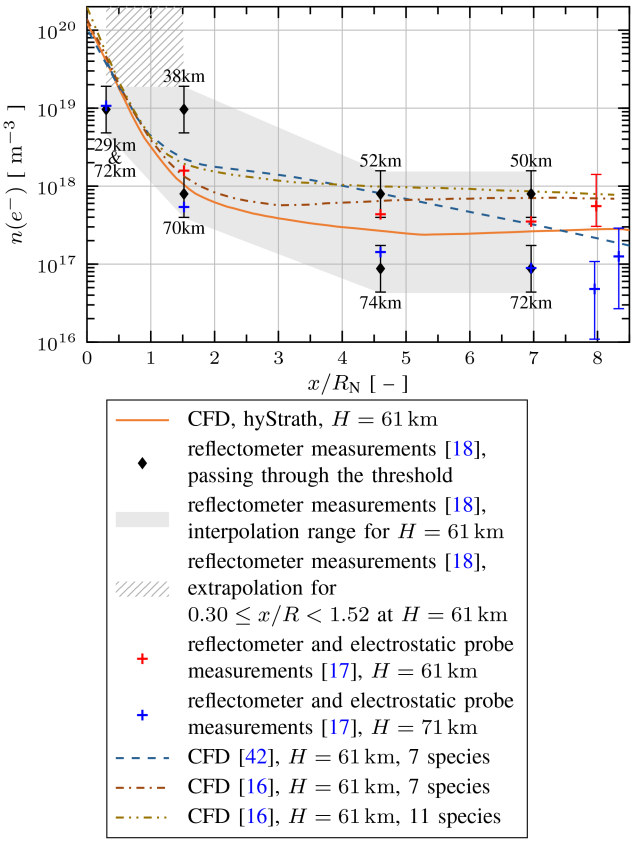

Fig. 10. Simulated maximum electron densities normal to the surface of the RAM C-II flight vehicle and comparison with reflectometer and electrostatic probe measurements [17], [18] as well as numerical simulations [16], [42] from the literature.

threshold at 72 km and was only falling below the threshold at 29-km altitude, rendering the electron number density for $x/R_N = 0.30$ higher than 10^{19}m^{-3} without any upper bound since no higher frequency signal was available. In Fig. 10, this is represented by the extrapolation range for $0.30 \leq x/R_N < 1.52$, while there is no range given for $x/R_N < 0.30$ and $x/R_N > 6.96$ due to the lack of any reflectometer data for these axial positions. Furthermore, the interpolations for and 71-km altitude as given by Jones and Cross [17] are in addition to electrostatic probe measurements at $x/R_N \approx 8.0$ and $x/R_N \approx 8.3$ corresponding to wall stand-off distances of 0.0096 and 0.0708 m, respectively [17].

Although using slightly different numerical approaches and boundary conditions, e.g., assuming wall temperatures of 1000 K [42] and 1200 K [16] compared to 1500 K of this study, all of the numerical simulations are in good agreement with the experimental data. The numerical results are even almost identical in the stagnation region ($x/R_N < 1$) and only start to deviate for $x/R_N > 1$. It has, for example, already been observed, that the use of lower number of species for the chemistry model reduces the electron number density downstream of the model shoulder [16], [43]. Hence, the use of an 11-species model instead of the 7-species model, would probably bring the numerical simulation result of this study even closer to the interpolated reflectometer data for 61-km altitude [17], although the

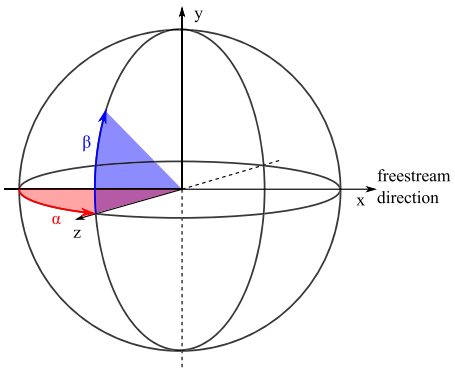

Fig. 11. Target-centered coordinate system with freestream orientation defining azimuth α and elevation β.

given measurement uncertainties do not allow to favor one of the simulation results over the others.

D. Simulated Freestream Conditions

To reduce the complexity of future computations by omitting the necessity of solving the nozzle flow first, all relevant freestream parameters including the simulated microscopic parameters are given in Table III. The presented values are the time and spatial average 20-mm upstream of the sphere stagnation point during the quasi-steady-state conditions 1.05 ms $\leq t \leq$ 1.25 ms. While the pressure p and density ρ averages are weighted only based on the varying flow cross section for the individual radial positions, Mach number Ma, translational-rotational and vibrational-electronic temperature T_t and T_v, respectively, and number densities $n(i)$ of the species i are weighted by both, flow cross section and density to account for the temporal and spatial density fluctuations of ±4% (standard deviation).

V. ELECTROMAGNETICS SIMULATION

Informed by the aerodynamic simulation, a subsequent electromagnetic simulation yields the prediction for the radar response of the emerging plasma sheath in each shock tunnel experiment. A detailed description of the preparation steps and the solver itself is given as follows.

A. Model and Solver

To simulate the interaction of microwave radiation like radar waves with cold, aerodynamic plasma, the plasma is modeled as a lossy dielectric medium with a complex permittivity (8) requiring the distributions of the plasma frequency f_P (9) and the collision frequency f_C (10), which are both derived from the aerodynamic simulation. To simulate the electromagnetic response, the FDTD solver in the *CST Microwave Studio* framework [44] was used. To evaluate the monostatic RCS, a Gaussian wideband plane wave excitation was applied. Corresponding to the geometry of the test scene, the aspect angle was set to $(\alpha, \beta) = (0°, 45°)$ in the target centered coordinate system (see Fig. 11). The monostatic RCS mode is designed for far-field analyses and does not take nearfield effects into account. In the nearfield, the RCS cannot be obtained by a simple r^{-2} relationship

TABLE III
Simulated Freestream Conditions

condition	Ma [-]	$\|U\|$ [$\mathrm{m\,s^{-1}}$]	p [Pa]	ρ [$\mathrm{g\,m^{-3}}$]	T_t [K]	T_v [K]	n(O_2) [$\mathrm{m^{-3}}$]	n(N_2) [$\mathrm{m^{-3}}$]
4	8.7	3687	232	1.80	433	1322	5.60E+21	2.90E+22
5	8.6	3718	243	1.80	444	1316	5.70E+21	2.90E+22
6	9.9	2752	62	1.10	190	1550	4.20E+21	1.80E+22
7	9.9	2820	154	2.70	202	1410	1.00E+22	4.20E+22
8	9.6	2985	136	2.00	237	1428	7.20E+21	3.10E+22
9	9.3	3150	129	1.60	279	1421	5.60E+21	2.50E+22
10	9.3	3182	128	1.50	287	1418	5.30E+21	2.40E+22
11	9.2	3227	121	1.40	298	1419	4.70E+21	2.20E+22
12	9.0	3387	139	1.40	340	1390	4.60E+21	2.20E+22
13	9.0	3451	153	1.40	358	1376	4.70E+21	2.30E+22
14	8.9	3497	176	1.60	373	1360	5.20E+21	2.50E+22

condition	n(O) [$\mathrm{m^{-3}}$]	n(N) [$\mathrm{m^{-3}}$]	n(NO) [$\mathrm{m^{-3}}$]	n(NO^+) [$\mathrm{m^{-3}}$]	n(e^-) [$\mathrm{m^{-3}}$]	k [$\mathrm{m^2\,s^{-2}}$]	ω [$\mathrm{s^{-1}}$]
4	2.10E+21	6.90E+11	2.60E+21	8.30E+14	6.90E+14	5.90E-03	2.50E+03
5	2.20E+21	7.30E+11	2.60E+21	8.70E+14	7.10E+14	5.20E-03	2.50E+03
6	1.80E+20	2.10E+10	1.30E+21	9.70E+13	9.70E+13	1.60E-02	2.40E+03
7	1.80E+20	1.30E+10	3.10E+21	1.20E+14	1.20E+14	3.50E-04	1.00E+03
8	3.60E+20	4.60E+10	2.50E+21	2.00E+14	2.00E+14	2.20E-03	1.60E+03
9	6.30E+20	1.30E+11	2.20E+21	3.10E+14	3.10E+14	7.80E-03	2.20E+03
10	6.90E+20	1.60E+11	2.10E+21	3.40E+14	3.30E+14	9.70E-03	2.40E+03
11	7.90E+20	2.10E+11	1.90E+21	3.70E+14	3.60E+14	1.70E-02	2.70E+03
12	1.20E+21	3.60E+11	2.00E+21	5.00E+14	4.70E+14	2.60E-02	2.90E+03
13	1.30E+21	4.30E+11	2.10E+21	5.60E+14	5.20E+14	2.10E-02	2.80E+03
14	1.50E+21	4.50E+11	2.30E+21	6.10E+14	5.50E+14	1.60E-02	2.60E+03

anymore, like it is realized in $H(r)$. However, due to the scatter of the calibration measurements in Fig. 7, no clear nearfield trend in the close region apart from the r^{-2}-law can be recognized. Instead, the r^{-2}-law still appears to be a reasonable choice for $H(r)$. This means that nearfield effects in the measurement region are not dominant and that a plane wave simplification is reasonable.

The spherical shell was modeled with a constant nondispersive complex permittivity according to the respective material Teflon (PTFE, $\epsilon_r = 2.1$, $\tan\delta = 0.0002$) and Polyamide (PA, $\epsilon_r = 2.33$, $\tan\delta = 0.011$), whereas for the plasma, the Drude model (8) was used. The FDTD solver *CST* requires a 3-D cubic mesh, which thus needs to be specifically generated.

B. Mesh

In Fig. 12, the final x–y cross-section grid is shown, where x denotes the flow direction from left to right (see Fig. 11). The 150-mm diameter spherical shell, with a wall thickness of 5 mm includes a concentric 140-mm diameter sphere of vacuum and is surrounded by a 200-mm cube defined as Drude material for hosting the plasma. To reduce reflections at the domain boundaries, the model is surrounded by a 50-mm vacuum background layer with a set of perfectly matched layers (PMLs) in all directions. The mesh is symmetric and has 350 cells in each direction (x, y, and z), which is 42 875 000 mesh cells in total. The smallest cell has a width of 0.625 mm and the largest 1.308 mm. Hence, there are no strong deviations in the cell size and the cells are overall much smaller than the smallest wavelength $\lambda(15\ \mathrm{GHz}) = 20$ mm. An example for the integration of the different materials in the mesh is given in Fig. 13. Here, a typical plasma frequency distribution is shown together with the PTFE spherical shell model. The size of the plasma cube is well chosen so that all relevant effects can be calculated inside and decay at the chosen boundaries. To study the grid dependence, the resolution

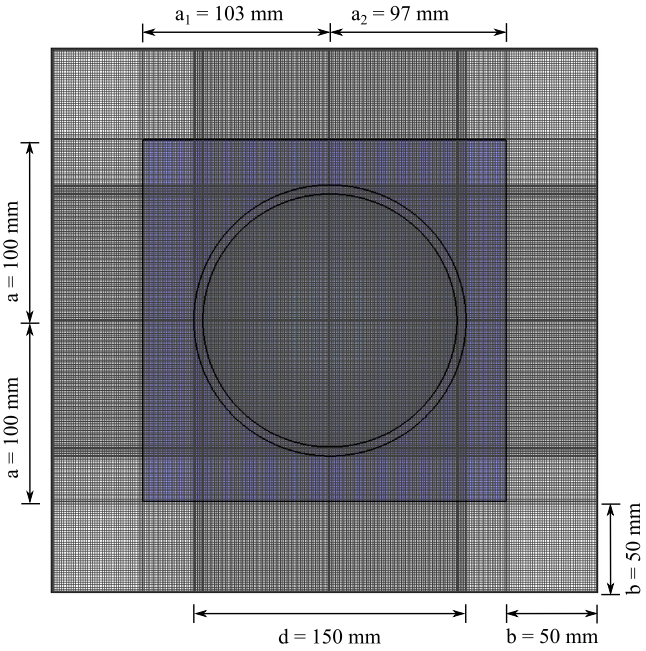

Fig. 12. x–y cross section of the cubic (hexahedral) mesh for the electromagnetic FDTD simulation. x–z cross-section analogous. Flow coming from the left with a denoting the half edge of the plasma cube, a_1 and a_2 the streamwise asymmetry, d the sphere diameter, and b the width of the PML background.

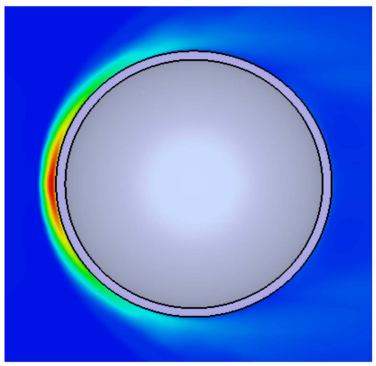

Fig. 13. Plasma frequency distribution in the cube region.

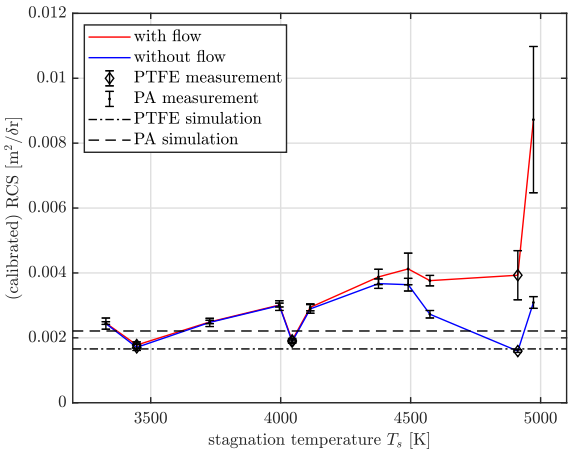

Fig. 14. Measured front reflection peaks as a function of the flow condition designated by the stagnation temperature T_s before and during the test time.

was increased from 1 to 0.6 mm and 0.3 mm. Despite a large increase of computational cost, only deviations of less than 1% in the front peak RCS were detected. The initial 1-mm grid appears, thus, sufficient for the given setup.

VI. EXPERIMENTAL RESULTS

A. Range Profile Analysis

In order to come up with a set of reusable reference data, the front reflection of the sphere in the 3 to 15-GHz band range profile is analyzed first. As stated previously, due to Fourier averaging, this value is less affected by noise, and thus, more stable and appears suitable for comparison with measured results. This is supported by Fig. 14, where the measured front reflection peaks are given. The values were averaged across the test time (red curve) with durations between 52 and 300 μs and compared to the average of the 200 μs before the flow arrival (blue curve). The errorbars represent the square standard deviation within these time intervals. The pure noise contribution is apparently insignificantly small as the blue curve errorbars show. A larger contribution of uncertainty comes from the standard deviation during the test time. Since it is only enlarged when the mean RCS peak value (red) differs from the reference (blue), it is likely to be a flow related feature.

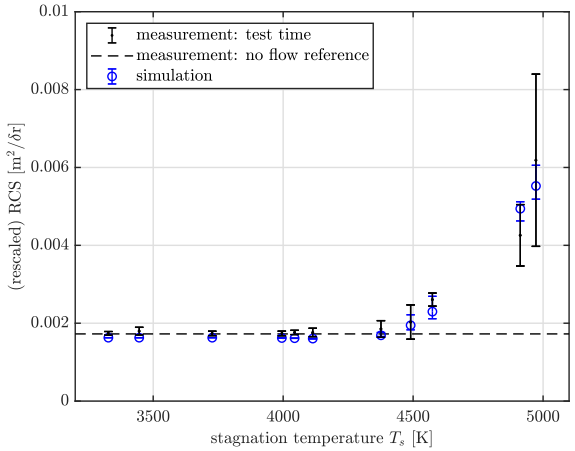

Fig. 15. Corrected front reflection peaks as a function of the flow condition designated by the stagnation temperature T_s in comparison with the simulation results.

This observation is supported by the camera footage, which shows brightness fluctuations in the same time interval. The largest fluctuation—the variance of the reference RCS (blue) between different shots, however, seems to be a systematic error (PA: $\sigma_{\text{sim}}^{\text{PA}} = 0.0022$ m^2; $\sigma_{\text{meas}}^{\text{PA}} = (0.0030 \pm 0.0005)$ m^2. The manufacturing tolerances of the sphere are far too low to explain these large differences. It is more likely that the experimental suspension of the sphere from the test section's ceiling was too inaccurate so that the assumptions on the aspect angle and the related calibration resulted in this increased scatter. For the PTFE spheres, this effect is weaker so that the simulation still produces a good estimation (PTFE: $\sigma_{\text{sim}}^{\text{PTFE}} = 0.0017$ m^2; $\sigma_{\text{meas}}^{\text{PTFE}} = (0.0017 \pm 0.0001)$ m^2). Following this argumentation and assuming that the front reflection RCS of the sphere is only a function of the material and that the scatter only originates from uncertainties in the positioning of the test model, the systematic scatter was compensated by the first term of

$$\sigma = \frac{\sigma}{\sigma_{\text{ref}}^{\text{mat}}} \left\langle \sigma_{\text{ref}}^{\text{mat}} \right\rangle - \delta^{\text{mat}} \cdot \left(\left\langle \sigma_{\text{ref}}^{\text{PA}} \right\rangle - \left\langle \sigma_{\text{ref}}^{\text{PTFE}} \right\rangle \right) \tag{21}$$

$$\delta^{\text{mat}} = \begin{cases} 1, & \text{for mat} = \text{PA} \\ 0, & \text{else} \end{cases} \tag{22}$$

whereas the second term removes the material difference between PA and PTFE. Here, it was assumed that the plasma influence is additive because the RCS increase is far from saturation. This is reasonable since in the fully overdense limit with infinite electron density, the spherical plasma sheath becomes practically a perfectly conducting sphere with a diameter of $D = 15$ cm. In the optical limit its RCS would be given by $\pi D^2/4 = 0.018$ m^2, which is an order of magnitude larger than the average RCS value without plasma. The results are shown in Fig. 15 together with the respective simulation results. Good agreement between simulation and experiment was achieved. Since the main systematic errors were absorbed by the scaling operation (21), the errorbars express the variance of the signal during the test time. It shows that the flow, which produces

the plasma, is not perfectly stable. This is also visible in the video footage, which shows significant oscillations in the emitted light coming from the stagnation region of the sphere. It is an effect that is possibly linked to freestream disturbances, which are inevitable side products of the way shock tunnels produce their high flow speeds. This is supported by the fact, that these oscillations in the freestream conditions are also present in the simulation. The simulated oscillations are indicated by the blue errorbars in Fig. 15, which, however, tend to be smaller than the measured ones but also grow with the flow enthalpy or stagnation temperature, respectively.

However, since these oscillations affect multiple parameters and since each parameter must obey different boundary conditions, the parameter values do not simply scale to a mean value in a linear way. Hence, there is the need to revise the definitions of the average and the measure for deviation. For the single amplitude value in the (1-D) radar measurement, it has just been the mean and the standard deviation of the amplitude value translated to the quadratic power measure RCS. For the aerodynamic case, at every point of the CFD grid, effective averages were formed being the arithmetic mean in each dimension, but, for simplicity, without respecting the governing physical boundary conditions. To estimate the width of the oscillations, a stationary flow region was identified first and afterwards the conditions at the time instant with the minimal and maximal electron density—the most important plasma parameter—were used. Hence, for each test run, three electromagnetic simulations were carried out: the aerodynamic simulation time instants with the minimum and the maximum electron density and an effective average, which does not necessarily represent a physical state. Since the results of this effective value are always between the maximum and minimum values (see Fig. 15), which indeed present physical states, the use of this effective stationary value appears reasonable.

B. Spectral Analysis

The frequency spectrum of the front reflection peak can be evaluated analogously to the analysis in the range profile. Since the back reflection and the surface and waveguide contributions lie behind the front reflection and are thus influenced by it, it is advantageous to consider only the front reflection peak spectrum. It can be obtained directly by the inverse Fourier transform of a window around the front reflection peak and is shown in Fig. 16. While, the order of magnitude and evolution with stagnation temperature agree well in measurement and simulation, there is still some deviation in the absolute values. These differences are most probably caused by the combination of uncertainties that were already discussed for the measurement of the front reflection peak: the positioning of the sphere, the signal variation during the test time, nearfield effects in the calibration, and maybe also the presence of heavy metal dust. For now, however, the influence of the latter must

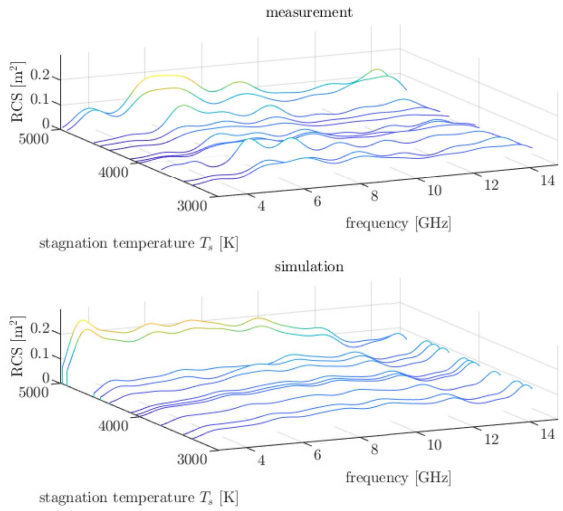

Fig. 16. Comparison of the measured and simulated RCS spectra of the front reflection peak.

remain unknown, but it should be investigated in subsequent studies.

Inspired by this observation, another attempt is made to visualize the plasma influence. Similar to the scaling before, the uncertainties in the absolute values are absorbed by a relative analysis, which is explained subsequently. Therefore, the underlying model for the interaction of electromagnetic waves with plasma is considered: the plasma dispersion relation (8). It describes the frequency dependence of plasma. As a general insight, the influence vanishes when the radar frequency f exceeds the plasma frequency f_P. This means f_P presents a cutoff in the spectrum. Since f_P is directly linked to the local electron density $n(e^-)$, an observed cutoff in the radar measurement indicates the presence of a corresponding electron density. The electron density $n(e^-)$ is determined by the flow conditions and emerges with the start of the flow and vanishes when the flow fades out. Since the generation of the hypersonic flow is a continuous process and the conditions are not established immediately but require some time, known as the nozzle starting process. Later, the parameters $n(e^-)$, and thus, f_P—the cut-off frequency—vary and reach a quasi-static state during the test time. For the radar measurement, this means, that the frequency range in the RCS spectrum affected by plasma will also vary across a shock tunnel run. The aforementioned discussion shows that lower frequencies should be disturbed, whereas higher ones remain unchanged. Observing this behavior would be clear evidence for the emergence of a dispersive medium in the flow, hence plasma.

Therefore, a descending cumulative sum of squares C^2 of the difference of measured RCS spectrum $S(t, f)$ was defined with respect to the average spectrum $\langle S_0(t, f)\rangle$ before the flow arrival at t_0 such that

$$C^2(t, f_L) = \sum_{l=L}^{L_1} |S\left(t, f_l\right) - \left\langle S_0(t', f_l)\right\rangle|^2 \tag{23}$$

$$\text{with} \quad f_{L_1} = f_0 + B, \quad t' < t_0. \tag{24}$$

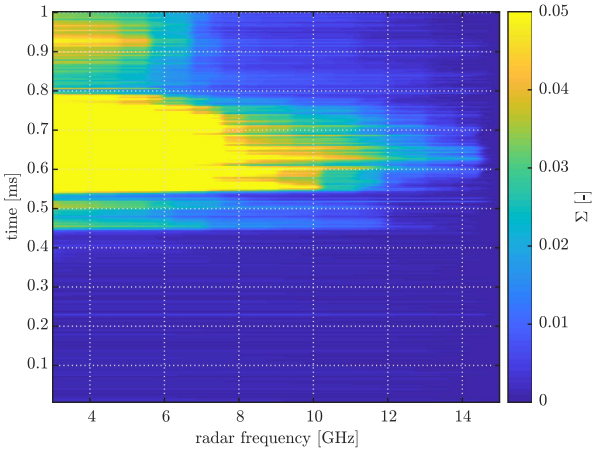

Fig. 17. Variation of the plasma influence on the frequency spectrum during shock tunnel run No. 5 visualized by the Σ-channel.

Relating this measure to the quadratic integral value before the flow arrival yields

$$\Sigma(t, f) = \frac{C^2(t, f)}{\sum_{l=1}^{L_1} \langle \hat{S}_0(t', f_l) \rangle^2}. \tag{25}$$

The Σ-channel accumulates differences between the altered spectrum and the spectrum before the flow arrival from higher to lower frequencies. Changes in the low-frequency region and invariance at higher frequencies can thus be visualized at the same time. Fig. 17 shows the Σ-channel for the shock tunnel run No. 5. The expected behavior is observed. The lower frequencies show pronounced deviations, whereas higher frequencies remain nearly unchanged. This presents a clear evidence for the presence of plasma in the flow.

A central parameter for the description of plasmas is the plasma frequency, and hence, the electron density. Although there is no clear cutoff frequency that could be identified with a single plasma frequency, in Fig. 17, there is a fading in the sigma channel that separates disturbed regions (yellow) from undisturbed ones (blue). Further, given the fact that the plasma frequency in the plasma sheath is rather a distribution than a single value (see Fig. 13), it is clear that also in the measurement, there is no single relevant plasma frequency but a distribution of plasma frequencies. To analyze the dependence between the Σ-channel and plasma frequency f_P in Fig. 18, the measurement and simulation of the Σ-channel are compared to the plasma frequency histogram. For the plasma frequency histogram, the number of aerodynamic simulation cells in the EM grid were counted, which host a certain plasma frequency. The frequency bin width was 50 MHz.

Some important observations were made here. First, the Σ-channel simulations agree well with the measurements, although locally there are some minor differences. It is likely, that these result from the uncertainties that already caused the bias in the front reflection range profile peak. Second, the simulated fading behavior also agrees well with

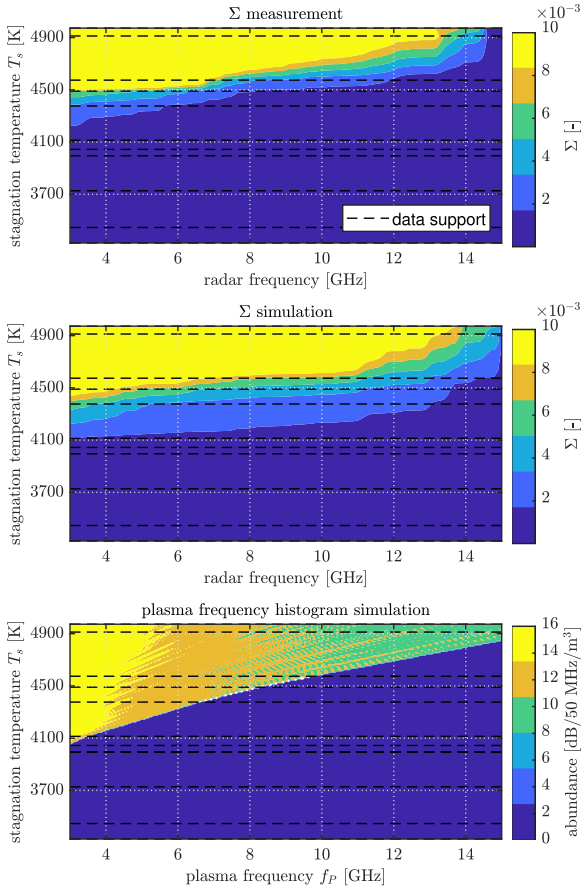

Fig. 18. Measured and simulated Σ-channels as a function of the flow condition designated by the stagnation temperature T_s. The dashed lines indicate the data base for the contour interpolation.

the measurement. Third, the Σ-channel shows the same distribution as the plasma frequency histogram. And finally, the maximum plasma affected frequency $f_{\max}$ increases with the stagnation temperature and the onset of this development coincides with the one observed for the front reflection peak RCS in Fig. 15. Summarizing, it appears reasonable to estimate the plasma frequency f_P, and thus, also the electron density $n(e^-)$ from the Σ-channel rise. Due to the fading, the uncertainty of this estimation lies in the range of a few gigahertz. The respective electron density $n(e^-)$ can be estimated with (9) as follows:

$$n(e^-) = 4\pi^2 f_{\max}^2 \frac{\epsilon_0 m_e}{e^2}. \tag{26}$$

To obtain an estimate for $f_{\max}$, the $\Sigma = \text{const.}$ isolines were calculated in Fig. 18. By definition, Σ relates the descending integral of the square deviation of the plasma disturbed spectrum from the undisturbed spectrum to the integral of the square of the undisturbed spectrum. Due to monotony, the total measured deviation is found at the lowest frequency $f = 3$ GHz. Hence, a threshold from where a spectrum is considered as disturbed can be derived from the Σ-channel in the time before the flow arrival. In this undisturbed region

$$\max_f \Sigma(f) = \Sigma(f = 3\text{GHz}) = (0.0014 \pm 0.006). \tag{27}$$

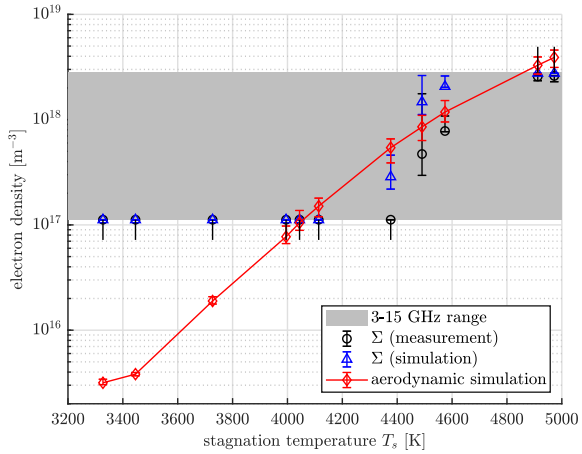

Fig. 19. Electron density estimation from the $\Sigma = 0.0044$ isoline compared to the maximum electron density in the aerodynamic simulation.

A typical level that is used for excluding events to originate from an underlying statistic process—here, noise—is the five-sigma threshold. It lies at $\Sigma = 0.0044$ and will subsequently serve as a detection threshold for significant plasma effects. The obtained estimates for the electron density are given in Fig. 19. Due to the limited bandwidth, the radar system (gray patch) can only detect cutoffs, i.e., plasma frequencies, in a certain frequency range. Since the plasma frequency is directly linked to the electron density, the system can only detect electron densities in this range (here, 1×10^{17} m^{-3} to 2×10^{18} m^{-3}). Apart from this, the detection of no effect indicates a lower electron density and a complete saturation indicates a higher electron density. In the graph, this additional information is given by respective arrow annotations at the edge of the grey area pointing up or down, respectively. As neutral reference, the maximum electron density calculated by the aerodynamic simulation of the 15-cm-sphere cases is given in red. Obviously, in the center of the frequency range, the electron density estimates are fair given that the plasma sheath hosts a distribution of electron densities and the red line only gives the calculated maximum. Values below the maximum electron density (red), as measured, are more likely since there is an increasing number of cells, and thus, space and potentially reflective area with less than the maximum electron density (see Fig. 18, bottom). However, the Σ-channel of the simulation overestimates the electron density. This may be a result of the plasma frequency presenting a cutoff frequency only in the first order, but there are still effects at higher frequencies if the collision frequency is nonzero, even though these are smaller. The detection of these might have lead to this overestimation in the simulation that actually uses the data from the aerodynamic simulation indicated by the red line.

Although the uncertainty in the presented electron density estimate appears high and this technique might rather be used for order-of-magnitude estimates, nonintrusive electron density measurement techniques in experimental aerodynamics are rare, if present at all. Hence, this technique could also be a valuable source of electron density reference data for aerodynamic simulations.

VII. CONCLUSION

The aim of this study was to investigate an experimental way to validate numerical radar signature predictions for targets at hypersonic speed. For this purpose, wind tunnel experiments with a sphere model were successfully conducted in a hypersonic shock tunnel at Mach 8. In a set of test runs, the flow conditions were varied such that plasma sheaths with different electron densities formed around the sphere model, which were measured with a monostatic radar setup in the frequency range from 3 to 15 GHz. In addition, both the distribution of the important plasma parameters—plasma frequency and collision frequency—and the respective response to an incident electromagnetic wave—the radar wave—were simulated numerically by combining aerodynamic and electromagnetic simulations. Good quantitative agreement was obtained especially in the radar range profiles. For the respective RCS frequency spectra and the electron density estimates, only good order of magnitude estimations were achieved.

Given these results, the application of radar in hypersonic shock tunnels for the investigation of high-speed plasma effects presents a valuable source of reference data for the validation of aerodynamic and electromagnetic simulations predicting radar signatures of hypersonic targets. Hence, all relevant values are given to foster independent simulations and to compare the results with the data given for the present experiments. Although, the accuracy of the raw data was rather limited, some systematic errors could be identified and corrected for so that the errors remain reasonable. However, for future experiments, the increase of measurement accuracy is one of the major tasks. Special attention will be paid to the positioning of the sphere and the calibration of the system.

This study only considers the rather simple case of a totally reflecting plasma around a stagnation point in hypersonic flow. To gain a deeper understanding of the relation between radar signatures and plasma sheath in hypersonic flow, future studies will need to address also other important flow phenomena and influencing factors like the effect of the size of the stagnation region, the presence of flaps or fins, the impact of laminar to turbulent boundary layer transition, the signature of the wake flow or the impact of ablation products in the flow. In some of these cases, it is likely that the RCS will—other than the case considered in this article—decrease by the presence of plasma. This will be another experimental challenge, but also gives an impression of the complexity of the topic.

ACKNOWLEDGMENT

The authors would like to thank ISL's shock tunnel team, namely B. Sauerwein (ISL), R. Kempf (ISL), and M. Bastide (ISL) for the lively support during the experiments; F. Leopold (ISL) for providing the experimental facilities; M. Warnke (FHR) for his dedicated support with the

experimental radar system and the related discussions; C. Salzburg (FHR) for his support of the electromagnetic simulations; and the team around J. M. Schramm (DLR), A. Wagner (DLR) and their team from the Spacecraft Department of the German Aerospace Center (DLR) in Götingen for the discussion that lead to the idea of this study.

REFERENCES

[1] J. Hruby, *Russia's New Nuclear Weapon Delivery Systems—An Open-Source Technical Review*, Nuclear Threat Initiative, Washington, DC, USA, 2019.

[2] R. H. Schmucker and M. Schiller, "Die Situation in den Ländern der Krisenregionen," in *Raketenbedrohung 2.0: Technische und Politische Grundlagen*, 1st ed. Hamburg, Germany: E. S. Mittler & Sohn, 2015, pp. 19–28.

[3] J. D. Anderson Jr., *Hypersonic and High-Temperature Gas Dynamics*, 2nd ed.Reston, VA, USA: AIAA, 2006.

[4] A. Piel, *Plasma Physics: An Introduction to Laboratory, Space, and Fusion Plasmas*, 1st ed. Berlin, Germany: Springer, 2017.

[5] G. Wang, L. Yuan, T. Wang, N. Fang, J. Miao, and B. Wang, "RCS calculation of complex targets shielded with plasma based on visual GRECO method," in *Proc. IEEE 3rd Int. Symp. Microwave, Antenna, Propag. EMC Technol. Wireless Commun.*, Beijing, China, 2009, pp. 950–953, doi: 10.1109/MAPE.2009.5355803.

[6] X. Zhang et al., "Establishment of a wideband radar scattering center model of a plasma sheath," *IEEE Access*, vol. 7, pp. 140402–140410, 2019, doi: 10.1109/ACCESS.2019.2943111.

[7] Y. Zhang, G. Xu, and Z. Zheng, "Terahertz waves propagation in an inhomogeneous plasma layer using the improved scattering-matrix method," *Waves Random Complex Media*, vol. 31, no. 6, pp. 2466–2480, 2021, doi: 10.1080/17455030.2020.1757177.

[8] Y. Ding et al., "An analysis of radar detection on a plasma sheath covered reentry target," *IEEE Trans. Aerosp. Electron. Syst.*, vol. 57, no. 6, pp. 4255–4268, Dec. 2021, doi: 10.1109/TAES.2021.3090910.

[9] V. F. Giangaspero et al., "3D ray tracing solver for communication blackout analysis in atmospheric entry missions," *Comput. Phys. Commun.*, vol. 286, 2023, Art. no. 108663, doi: 10.1016/j.cpc.2023.108663.

[10] H. Deng, X. Wei, and H. Yin, "EM scattering analysis of complex target coated with plasma by conformal SO-FDTD method," in *Proc. IEEE Int. Conf. Green Comput. Commun. IEEE Internet Things IEEE Cyber, Phys. Soc. Comput.*, Beihang, China, 2013, pp. 1538–1541, doi: 10.1109/GreenCom-iThings-CPSCom.2013.273.

[11] H. Sun et al., "Backward scatttering characteristics of a reentry vehicle enveloped by a hypersonic flow field," *Int. J. Antennas Propag.*, vol. 2018, 2018, Art. no. 5478580, doi: 10.1155/2018/5478580.

[12] Y. Wang, S. Liu, and S. Zhong, "Studies on the effects of the plasma wake flow fields of hypersonic reentry blunt cone on electromagnetic wave," *IEEE Plasma Sci.*, vol. 47, no. 8, pp. 3991–3996, Aug. 2019, doi: 10.1109/TPS.2019.2926166.

[13] Y. Takahashi, "Propagation path of radio waves in nonequilibrium reentry plasma around a nanosatellite with an inflatable aeroshell," *IEEE Trans. Aerosp. Electron. Syst.*, vol. 58, no. 5, pp. 4070–4082, Oct. 2022, doi: 10.1109/TAES.2022.3158625.

[14] R. N. Gupta, J. M. Yos, R. A. Thompson, and K. P. Lee, "A review of reaction rates and thermodynamic and transport properties for an 11-species air model for chemical and thermal nonequilibrium calculations to 30000 K," NASA, Washington, DC, USA, NASA-RP-1232, 1990.

[15] C. Park, "Review of chemical-kinetic problems of future NASA missions. I.—Earth entries," *J. Thermodynamics Heat Transfer*, vol. 7, no. 3, pp. 385–398, Jul. 1993, doi: 10.2514/3.431.

[16] P. Sawicki, R. Chaudhry, and D. Boyd, "Influence of chemical kinetics models on plasma generation in hypersonic flight," *AIAA J.*, vol. 60, no. 1, pp. 31–40, 2022, doi: 10.2514/1.J060615.

[17] W. L. Jones Jr and A. E. Cross, "Electrostatic-probe measurements of plasma parameters for two reentry flight experiments at 25000 foot per second," Langley Research Center, NASA, Hampton, VA, USA, NASA-TN-D-6617, 1972.

[18] W. L. Grantham, "Flight results of a 25,000 ft/sec reentry experiment using microwave reflectometers to measure plasma electron density and standoff distance," Langley Research Center, NASA, Hampton, VA, USA, NASA-TN-D-6062, 1970.

[19] M. G. Dunn and S. Kang, "Theoretical and experimental studies of reentry plasmas," NASA, Washington, DC, USA, NASA-CR-2232, 1973.

[20] W. L. Darnell, "Radar cross section and optical radiation from the Trailblazer IIa 9°half-angle blunt nose cose during hypersonic reentry," Langley Research Center, NASA, Hampton, VA, USA,NASA-TN-D-3214, 1966.

[21] S. Close, M. Oppenheim, S. Hunt, and L. Dyrud, "Scattering characteristics of high-resolution meteor head echoes detected at multiple frequencies," *J. Geophys. Res.*, vol. 107, no. A10, 2002, Art. no. 1295, doi: 10.1029/2002JA009253.

[22] L. Dyrud et al., "Plasma and electromagnetic simulations of meteor head echo radar reflections," *Earth, Moon, Planets*, vol. 102, pp. 383–394, Jun. 2008, doi: 10.1007/s11038-007-9189-8.

[23] O. Igra and F. Seiler, *Experimental Methods of Shock Wave Research*, 1st ed. Cham, Switzerland: Springer, 2016.

[24] K. Chadwick, D. Boyer, and S. Andre, "Plasma and flowfield induced effects on hypervelocity re-entry vehicles for l-band irradiation at near broadside aspect angles," in *Proc. 27th Plasma Dyn. Lasers Conf.*, Jun. 1996, Art. no. 2322.

[25] C. Laviron, A. J. H. Donná, M. E. Manso, and J. Sanchez, "Reflectometry techniques for density profile measurements on fusion plasmas," *Plasma Phys. Control. Fusion*, vol. 38, pp. 905–936, Mar. 1996.

[26] B. Jiang et al., "Contactless measurement of hypervelocity projectile wake velocity distribution," *IEEE Access*, vol. 7, pp. 28968–28972, 2019, doi: 10.1109/ACCESS.2019.2894175.

[27] R. Petervari, A. Nekris, and T. Bieker, "Numerical analysis of radar-plasma-signatures of a sphere in a mach 10 hypersonic wind tunnel flow," in *Proc. 18th Eur. Radar Conf.*, London, U.K., 2022, pp. 86–89.

[28] K. L. Wray, J. D. Teare, B. Kivel, and P. Hammerling, "Relaxation processes and reaction rates behind shock fronts in air and component gases," in *Proc. Symp. (Int.) Combustion*, Jan. 1961, pp. 328–339.

[29] M. Gunar and R. Menella, "Signature studies for a re-entry system," in *Proc. Space Congr. Proc.*, 1965, pp. 515–548.

[30] P. Gnemmi et al., "Shock tunnels at ISL," in *Experimental Methods of Shock Wave Research*, 1st ed. Cham, Switzerland: Springer, 2016, pp. 131–180.

[31] B. A. Cruden, C. Y. Tang, J. Olejniczak, A. J. Amar, and H. Tanno, "Characterization of radiative heating anomaly in high enthalpy shock tunnels," *Exp. Fluids*, vol. 62, 2021, Art. no. 142, doi: 10.1007/s00348-021-03227-2.

[32] U.S. Standard Atmosphere, 1976, NASA, U. S. Air Force, Washington, DC, USA, NOAA-S/T76-1562, 1976.

[33] M. K. McIntosh, "Computer program for the numerical calculation of frozen and equilibrium conditions in shock tunnels," Dept. Phys., Australian National Univ., Canberra, Australia, Tech. Rep. CR-181721, 1968.

[34] F. R. Menter, "Two-equation Eddy-viscosity turbulence models for engineering applications," *AIAA J.*, vol. 32, pp. 1598–1605, 1994, doi: 10.2514/3.12149.

[35] V. Casseau, "An open-source CFD solver for planetary entry," Ph.D. dissertation, Dept. Mech. Aerospace Eng., Univ. Strathclyde, Glasgow, U.K., 2017.

[36] F. G. Blottner, M. Johnson, and M. Ellis, "Chemically reacting viscous flow program for multi-component gas mixtures," Sandia Labs., Albuquerque, NM, USA, Tech. Rep. SC-RR-70-754, 1971.

[37] S. Chapman and T. G. Cowling, *The Mathematical Theory of Non-Uniform Gases: An Account of the Kinetic Theory of Viscosity, Thermal Conduction, and Diffusion in Gases*. Cambridge, U.K.: Cambridge Univ. Press, 1939.
[38] B. F. Armaly and K. Sutton, "Viscosity of multicomponent partially ionized gas mixtures," in *Proc. 15th Thermophysics Conf.*, Snowmass, CO, USA, 1980, p. 1495.
[39] R. N. Gupta, J. M. Yos, and R. A. Thompson, "A review of reaction rates and thermodynamic and transport properties for an 11-species air model for chemical and thermal nonequilibrium calculations to 30000 K," Langley Research Center, NASA, Hampton, VA, USA, NASA-TM-101528, 1989.
[40] J. D. Anderson Jr., *Fundamentals of Aerodynamics*. New York, NY, USA: McGraw-Hill, 2001.
[41] G. Tchuen and D. E. Zeitoun, "Computation of weakly ionized air flow in thermochemical nonequilibrium over sphere–cones," *J. Heat Fluid Flow*, vol. 29, pp. 1393–1401, 2008, doi: 10.1016/j.ijheatfluidflow.2008.06.002.
[42] G. V. Candler and R. W. MacCormack, "Computation of weakly ionized hypersonic flows in thermochemical nonequilibrium," *J. Thermophys. Heat Transfer*, vol. 5, no. 3, pp. 266–273, 1991, doi: 10.2514/3.260.
[43] S. F. Gimelshein and I. J. Wysong, "Impact of the ionization reaction set in nonequilibrium hypersonic air flows," *AIAA J.*, vol. 58, no. 3, pp. 1255–1265, 1991, doi: 10.2514/1.J058895.
[44] *CST Microwave Studio, CST Studio Suite Documentation*, Dassault Systèmes, Vélizy-Villacoublay, France, 2021.

René Petervari received the master's degree in physics from the University of Göttingen, Göttingen, Germany, in 2016. He is currently working toward the Ph.D. degree in radar systems engineering with the Faculty of Electrical Engineering and Information Technology, RWTH Aachen University, Aachen, Germany, investigating the influence of plasma sheath on radar signatures .

During his studies, he specialized on aerothermodynamics, and from 2013 onward, he assisted wind tunnel experiments at the local site with the German Aerospace Center. After his time in Göttingen, he joined the Fraunhofer Institute for High Frequency Physics and Radar Techniques in 2016 as a Research Associate in the field on noncooperative target recognition.

Stephan Weidner received the B.Sc., M.Sc., and Ph.D. degrees in mechanical engineering from the Karlsruhe Institute of Technology, Karlsruhe, Germany, in 2011, 2014, and 2019, respectively.

During his studies, he specialized in numerical methods for continuum mechanics and fluid dynamics, while extending his expertise to experimental fluid dynamics in his Ph.D. studies. Since 2014, he has been working in the field of aerodynamics, measurements, and simulations with the French-German Research Institute of Saint-Louis, Saint-Louis, France, where since 2019, he has been a Research Associate. His Ph.D. project resulted in publications in *AIAA Journal* and *Journal of Fluid Mechanics*. His research interests include experimental and numerical analysis of both, sub- to supersonic separated flows, and hypersonic nonequilibrium flow fields.

Alexander Nekris received the diploma degree in mechanical and process engineering from the Technical University of Kaiserslautern, Kaiserslautern, Germany, in 2014, and the Ph.D. degree in aerospace engineering from the Faculty of Aerospace Engineering, Bundeswehr University Munich, Neubiberg, Germany, in 2020.

From 2010 to 2014, he was a Research Assistant with the Department of Design and Construction of Machines and Apparatus, Technical University of Kaiserslautern. From 2014 to 2019, he was a Research Assistant in the fields of aerothermodynamics and finite-rate chemical kinetics in high-speed flows with the French-German Research Institute of Saint-Louis (ISL), Saint-Louis, France. Between 2019 and 2021, he was a Research Associate with the ISL within the same fields and a freelance OpenFOAM consultant. Since 2021, he is a Simulation Engineer with Agilent Technologies, Waldbronn, Germany. His research interests include fluid dynamics, thermodynamics, electrodynamics, and chemical kinetics.

Stefan Brüggenwirth (Senior Member, IEEE) received the diploma degree in aerospace engineering with specialization in computer science and space systems from the University of Stuttgart, Stuttgart, Germany, in 2008, and the Ph.D. degree in aerospace engineering from the Faculty of Aerospace Engineering, Bundeswehr University Munich, Neubiberg, Germany, in 2015.

He spend two and a half years years with NASA Ames Research Center and joined as the Head of the Cognitive Radar Department, Fraunhofer Institute for High Frequency Physics and Radar Techniques, Wachtberg, Germany, in 2014. His research interests include noncooperative target recognition, machine learning, and advanced signal processing for cognitive radar applications.

He is a NATO SET Panel member at large for machine learning and artificial intelligence in RF sensors.

Peter Knott has received the diploma and Ph.D. degrees in electrical engineering from RWTH Aachen University, Aachen, Germany, in 1994 and 2003, respectively.

In 1994, he joined the Fraunhofer Institute for High Frequency Physics and Radar Techniques (FHR) (formerly FGAN e.V.), Wachtberg, Germany. From 2005 to 2016, he was the Head of the Department Antenna Technology and Electromagnetic Modelling (AEM), where the focus of his work was on the design and development of antenna arrays and active antenna front-ends as well as electromagnetic modeling and beamforming methods for conformal antenna arrays. Since 2016, he has been the Executive Director with the FHR. He is also currently holding a professorship in radar systems engineering with RWTH Aachen University, and is a Lecturer with different other organizations. As part of his scientific activities, he has authored and co-authored numerous papers in scientific journals and at conferences, including several patents.

Dr. Knott is currently an expert with AESA Radar on the Sensors and Electronics Technology (SET) Panels of the NATO Science and Technology Organisation (STO) and a Member of the Brussels Advisory Board of the German Defence Technology Society (DWT). He was Co-Chair of the 14th European Radar Conference (EuRAD) in Nuremberg in 2017 and the Chair of the International Radar Symposium (IRS) from 2018 to 2023. From 2014 to 2019, he was also the Chairman of the Executive Committee of IEEE MTT/AP Joint Chapter, the Chairman of the VDE/ITG Technical Committee HF4 "Localisation," and a Member of the Scientific Advisory Board of the German Society for Localisation and Navigation (DGON) e.V.